

Electronic Structure and Magnetic Properties of the Half-metallic Ferrimagnet Mn_2VAl Probed by Soft X-ray Spectroscopies

K. Nagai,¹ H. Fujiwara,^{1,*} H. Aratani,¹ S. Fujioka,¹ H. Yomosa,¹ Y. Nakatani,¹
 T. Kiss,¹ A. Sekiyama,¹ F. Kuroda,^{2,3,4} H. Fujii,^{3,4} T. Oguchi,^{3,4} A. Tanaka,² J.
 Miyawaki,^{5,6} Y. Harada,^{5,6} Y. Takeda,⁷ Y. Saitoh,⁷ S. Suga,⁴ and R. Y. Umetsu⁸

¹*Graduate School of Engineering Science, Osaka University, Toyonaka, Osaka 560-8531, Japan*

²*Department of Quantum Matter, ADSM, Hiroshima University, Higashi-hiroshima, Hiroshima 739-8530, Japan*

³*CMI²-MaDIS, National Institute for Materials Science, 1-2-1 Sengen, Tsukuba, Ibaraki 305-0047, Japan*

⁴*Institution of Scientific and Industrial Research,
 Osaka University, Ibaraki, Osaka 567-0047, Japan*

⁵*Institute for Solid State Physics (ISSP), University of Tokyo, Kashiwanoha, Chiba 277-8581, Japan*

⁶*Synchrotron Radiation Research Organization, University of Tokyo, Sayo-cho, Sayo, Hyogo 679-5198, Japan*

⁷*Materials Sciences Research Center, Japan Atomic Energy Agency (JAEA), Sayo, Hyogo 679-5148, Japan*

⁸*Institute for Materials Research, Tohoku University, 2-1-1 Katahira, Sendai 980-8577, Japan*

(Dated: June 17, 2021)

We have studied the electronic structure of ferrimagnetic Mn_2VAl single crystals by means of soft X-ray absorption spectroscopy (XAS), X-ray absorption magnetic circular dichroism (XMCD) and resonant soft X-ray inelastic scattering (RIXS). We have successfully observed the XMCD signals for all the constitute elements. The Mn $L_{2,3}$ XAS and XMCD spectra are reproduced by spectral simulations based on density-functional theory, indicating the itinerant character of the Mn $3d$ states. On the other hand, the V $3d$ electrons are rather localized since the ionic model can qualitatively explain the V $L_{2,3}$ XAS and XMCD spectra. This picture is consistent with local dd excitations revealed by the V L_3 RIXS.

PACS numbers: 71.20.Be,75.50.Gg,78.70.Dm

INTRODUCTION

Half-metals are characterized by a peculiar electronic structure as one of the spin sub-bands is metallic and the other is semiconducting with a gap at the Fermi level (E_F). The expected 100% spin-polarization at E_F is suitable for functional spintronic applications. In particular, full-Heusler alloys with the chemical formula X_2YZ (X and Y : transition metals, Z : main group element) have been extensively studied since the Currie temperature (T_C) is, for example, as high as 985 K for Co_2MnSi [1, 2].

$L2_1$ ordered Mn_2VAl is a ferrimagnet with $T_C \sim 760$ K [3, 4], and is predicted to be half-metallic [5, 6]. The saturation magnetic moment (M_s) is reported as $1.94 \mu_B$ per formula unit (f.u.) for poly crystalline samples [4, 7], which is much smaller than that of $4.78 \mu_B/\text{f.u.}$ for Co_2MnSi [8]. The small M_s due to the antiparallel spin coupling of V and Mn offers an advantage for saving the electric power of the current-induced magnetization switching, since the switching current is proportional to M_s^2 [9, 10].

To reveal the detailed magnetic properties and the electronic structure of the Heusler alloys, intensive studies have been performed by means of X-ray absorption spectroscopy (XAS) and X-ray absorption magnetic circular dichroism (XMCD) [11–19]. The electronic structure of Co_2MnSi has been known as the Co $3d$ electrons are itinerant, while the Mn $3d$ electrons contribute to the local magnetic moment [13, 14, 17]. Nevertheless, only few

works have been performed on Mn_2VAl [20–22] because of the difficulty in synthesizing high quality crystals. It has been reported as the epitaxially grown Mn_2VAl films are prone to various disorder [20]. Since the disorder effects change the magnetic properties and the local electronic structure [21], the line shapes of XAS and XMCD spectra varied depending on the individual samples [20–22]. Therefore, the electronic structure of Mn_2VAl is still controversial.

In this work, we present the detailed electronic structure and magnetic properties of the high quality single crystals of $L2_1$ -ordered Mn_2VAl , revealed by means of XAS and XMCD for all constitute elements. The magnetic moments of the Mn sites evaluated by using the magneto-optical sum-rule [23, 24] were qualitatively consistent with the results of density functional theory (DFT) within the experimental accuracy. We found that the line shapes of Mn $L_{2,3}$ XAS and XMCD spectra of Mn_2VAl were deviated from those of Mn spectra in Co_2MnSi , and are well explicable by the spectral simulation based on DFT, indicating the itinerant character of the Mn $3d$ electrons. On the other hand, the V $L_{2,3}$ XAS and XMCD spectra were qualitatively described in the ionic model. Moreover, the dd excitation in the V $3d$ states was probed using resonant soft-X-ray inelastic scattering (RIXS) [25, 26], suggesting that the V $3d$ electrons are localized.

EXPERIMENTAL

Characterization of single crystals

Polycrystalline mother ingots of Mn_2VAl and Co_2MnSi were prepared by induction melting in an argon gas atmosphere. Since the melting temperature of V is very high as ~ 2180 K and the vapor pressure of V is high enough during the induction melting process, the excess Mn ions are contained in the mother ingot of Mn_2VAl . Single crystals of both Mn_2VAl and Co_2MnSi were grown by the Bridgeman method with a size of 12 mm in diameter and about 30 mm in length. Obtained ingots were annealed at 1473 (1373) K in the case of Mn_2VAl (Co_2MnSi) to gain the size of single crystal grains. For Mn_2VAl , a two-step annealing process at 1123 K and 873 K was employed and the crystal was finally slow-cooled to room temperature to control the degree of order. The specimen of Co_2MnSi was obtained by slow cooling from 1373 K to room temperature. Crystal orientation was checked with a Laue camera and the specimen was cut in a strip form in the direction parallel to $\langle 100 \rangle$ for Mn_2VAl and $\langle 110 \rangle$ for Co_2MnSi . Composition of the specimens was confirmed with an electron probe microanalyzer (EPMA) to be Mn: 50.5, V: 26.9, Al: 22.6 for Mn_2VAl and Co: 50.0, Mn: 25.9, Si: 24.1 for Co_2MnSi . Moreover, the long-range order parameter for the L_{21} structure ($S_{L_{21}}$) [27, 28] was evaluated as 0.84 for Mn_2VAl and 0.90 for Co_2MnSi by using the X-ray diffraction measurements. Note that the $S_{L_{21}}$ value for Mn_2VAl was much higher than that for the epitaxial films of $S_{L_{21}} \sim 0.5$ [20, 21], indicating the well ordered single crystal.

The bulk magnetization was measured with a superconducting quantum interface device (SQUID) magnetometer. We obtained a total magnetic moment of $m_{\text{SQUID}} = 1.82 \mu_{\text{B}}/\text{f.u.}$ for Mn_2VAl single crystals, which is slightly smaller than the value of $1.94 \mu_{\text{B}}/\text{f.u.}$ for polycrystalline samples [4, 7] and the expected value of $2 \mu_{\text{B}}/\text{f.u.}$ from the Slater-Pauling rule [1]. This deviation would be due to off-stoichiometric effects; the small amount of excess Mn and V ions substituted into Al sites can reduce the total magnetic moment, (see APPENDIX).

Soft X-ray spectroscopies

Single crystalline samples were fractured *in situ* in ultrahigh vacuum to obtain the clean surface. XAS and XMCD measurements were performed at BL23SU in SPring-8 [29]. The spectra were recorded in total-electron-yield mode with an energy resolution better than 0.1 eV using a superconducting magnet in fields up to 2 T along the incident beam direction. To eliminate any experimental artifacts arising from system errors, each XMCD spectrum was measured for opposite orientations

of the applied magnetic field and the resulting spectra were averaged. The measurement temperature was set to 20 K. The RIXS measurements were performed at the SPring-8 BL07LSU ‘HORNET’ end-station [30–32]. The total energy resolution was set to ~ 200 meV at the measurement temperature of 300 K.

DENSITY FUNCTIONAL THEORY

The electronic structure calculation based on DFT has been performed using the HiLAPW code, which is based on the all-electron full-potential augmented plane-wave (FLAPW) method [33]. The generalized gradient approximation (GGA) using the Perdew-Burke-Ernzerhof scheme has been used for the exchange correlation potential [34, 35]. We have used the second-variation procedure to include the spin-orbit coupling in addition to a scalar-relativistic scheme, giving an accurate description equivalent to solving the Dirac equation for relatively light elements as $3d$ transition metals. Plane-wave expansion cutoffs were set to 20 Ry for wave functions and 80 Ry for charge density and potential functions. The muffin-tin sphere radius was chosen as 1.1 Å for all elements. For the Brillouin-zone integration, a $16 \times 16 \times 16$ mesh was used with the tetrahedron integration technique. The atoms were placed on the general form X_2YZ of the L_{21} structure with X at $(\frac{1}{4}, \frac{1}{4}, \frac{1}{4})$ and $(\frac{3}{4}, \frac{3}{4}, \frac{3}{4})$, Y at $(0, 0, 0)$, and Z at $(\frac{1}{2}, \frac{1}{2}, \frac{1}{2})$. The lattice constant was set to 5.875 Å [6].

Figure 1(a) shows the calculated spin-polarized density of states for Mn_2VAl with a half-metallic gap for the majority-spin states, which is qualitatively consistent with previous reports [5, 6]. The partial density of states (PDOS) in Figs. 1(b) and 1(c) show that the Mn $3d$ minority-spin sub-bands contribute mainly to the states in the vicinity of E_{F} . Meanwhile, PDOS of the V $3d$ states are only $\sim 10\%$ of PDOS of the Mn $3d$ states around E_{F} as shown in the insets. Clear splitting of the V $3d$ states into the occupied t_{2g} and unoccupied e_g states is seen with the band splitting energy of ~ 3.2 eV as shown in Fig. 1(d). The PDOS of the Al $3p$ states are even smaller and $\sim 10\%$ of the PDOS of the V $3d$ states at E_{F} .

The whole XMCD spectra were simulated within the dipole approximation on the basis of the FLAPW method, where the transition matrix elements were calculated only within the muffin-tin sphere. The core-hole potential in the final states was neglected in the present calculations. To take into account the experimental core-hole lifetime broadening, the calculated spectra were broadened using Lorentzian functions with $\gamma = 0.97(0.36)$ eV and $0.78(0.28)$ eV for the $L_2(L_3)$ edges of Mn and V, respectively, while 0.15 eV was employed for the Al K edge. The detailed information about the calculation has been given in Ref. 36.

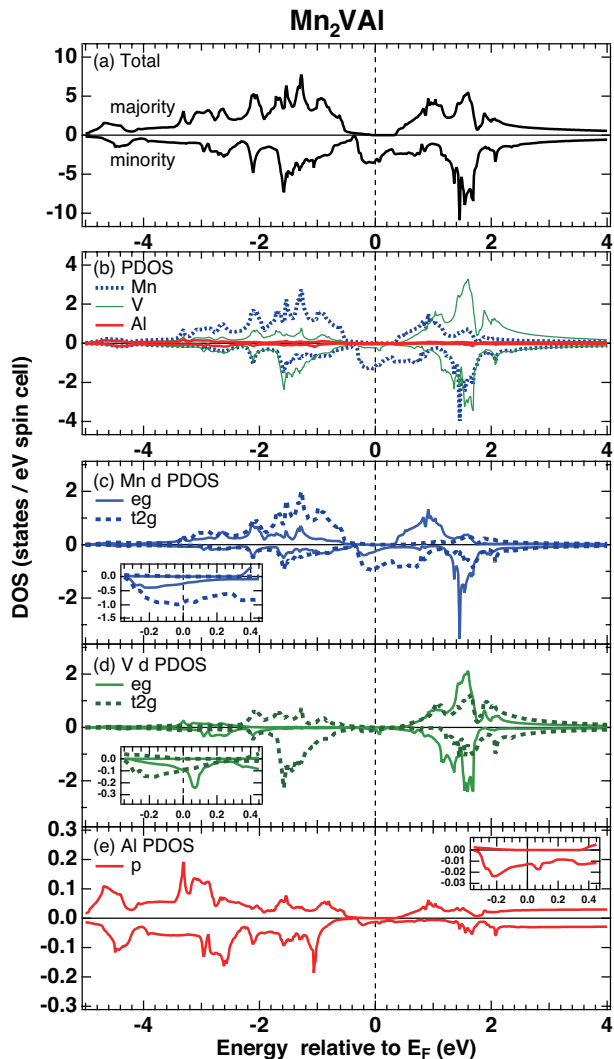


FIG. 1: (Color online) (a) Total density of states of $L_{2,3}$ ordered Mn_2VAI . (b) PDOS of Mn, V, Al sites. (c), (d) PDOS of Mn and V $3d$ states projected onto the e_g and t_{2g} orbital. (e) PDOS of Al $3p$ states. The insets show the enlarged view of PDOS around E_F .

RESULTS AND DISCUSSIONS

Magnetic properties probed by XMCD and sum-rule analysis

Figures 2(a) and 2(b) show the experimental results of Mn and V $L_{2,3}$ XAS and XMCD spectra of Mn_2VAI . μ^+ (μ^-) denotes the XAS absorption intensity for parallel (antiparallel) alignment of the photon helicity and sample magnetization direction. The XAS spectra are normalized by the L_3 peak intensity of the polarization-summed XAS ($\mu^- + \mu^+$). There are fine structures in the XMCD ($\mu^- - \mu^+$) spectra for both Mn and V $L_{2,3}$ edges, and the sign of the XMCD signals is opposite between them, reflecting ferrimagnetic coupling between the Mn

and V spins (Mn along applied field). The detailed line shape is discussed in the next subsection (IV. B).

Moreover, we can clearly see sizable XMCD signals even in the Al K edge as shown in Fig. 2(c) despite its non-magnetic atomic character [37, 38], indicating a non-negligible orbital polarization of the valence states with Al $3p$ character. The most prominent XMCD peak is located just at the threshold. The XMCD signals originate from a combination of the spin-orbit and exchange splittings of the Al $3p$ states. The integration of the XMCD signals over the K edge, which is proportional to the orbital magnetic moment [25, 39], falls to zero within the experimental accuracy.

The theoretical simulations are consistent with the experimental spectra, although there are some discrepancies in XMCD. The DFT calculation yields an orbital moment of $m_L = 0.001 \mu_B/Al$ with an orbital-to-spin magnetic moment ratio of $m_L/m_S = -0.05$. The deviation between the experiment and theory especially on the higher energy region is possibly due to the energy dependent lifetime broadening effects, which are not taken into account in the simulation, since the broadening width is given by fitting the edge step of the XAS spectrum.

To reveal more detailed magnetic properties of the transition metal sites, the orbital and spin magnetic moments per d hole were estimated by applying the magneto-optical sum-rule [23, 24, 40, 41] using the equations,

$$\frac{m_{spin}}{n_h} = -\frac{6p - 4q}{rP_c}C, \quad (1)$$

$$\frac{m_{orb}}{n_h} = -\frac{4q}{3rP_c}, \quad (2)$$

where n_h is the number of unoccupied d holes, p (q) is the integral of the XMCD signal over the $L_3(L_{2,3})$ -edge, and r is the integral of the polarization summed XAS intensity after subtracting the background. As shown in the bottom of Figs. 2(a) and 2(b), the cut off energy to obtain p was set to the minimum of the polarization summed XAS intensity between the L_2 and L_3 -edges. The q and r values were evaluated at the energy of 694 eV for Mn and 570 eV for V. P_c denotes the degree of circular polarization of 0.97 [29]. In addition, we must take into account the so-called jj mixing effect by using the correction factor C for the spin sum-rule [42]. Assuming $C = 1.5$ for Mn[43], we obtained a spin (orbital) magnetic moment of m_{spin}^{Mn} (m_{orb}^{Mn}) = 0.27 (0.005) $\mu_B/Mn/hole$, which is consistent with that obtained with our DFT calculation as summarized in Table I. Assuming $n_h = 5.20$ estimated from the DFT, we obtained a total Mn moment of 2.86 $\mu_B/f.u.$

Using the orbital sum-rule for V, we obtained an orbital magnetic moment of $m_{orb}^V = 0.005 \mu_B/V/hole$ as given in Table I. Meanwhile, it is not straight forward to adopt the spin sum-rule for V since the C value is not established and ranges from 3.6 to 5.0 due to the small

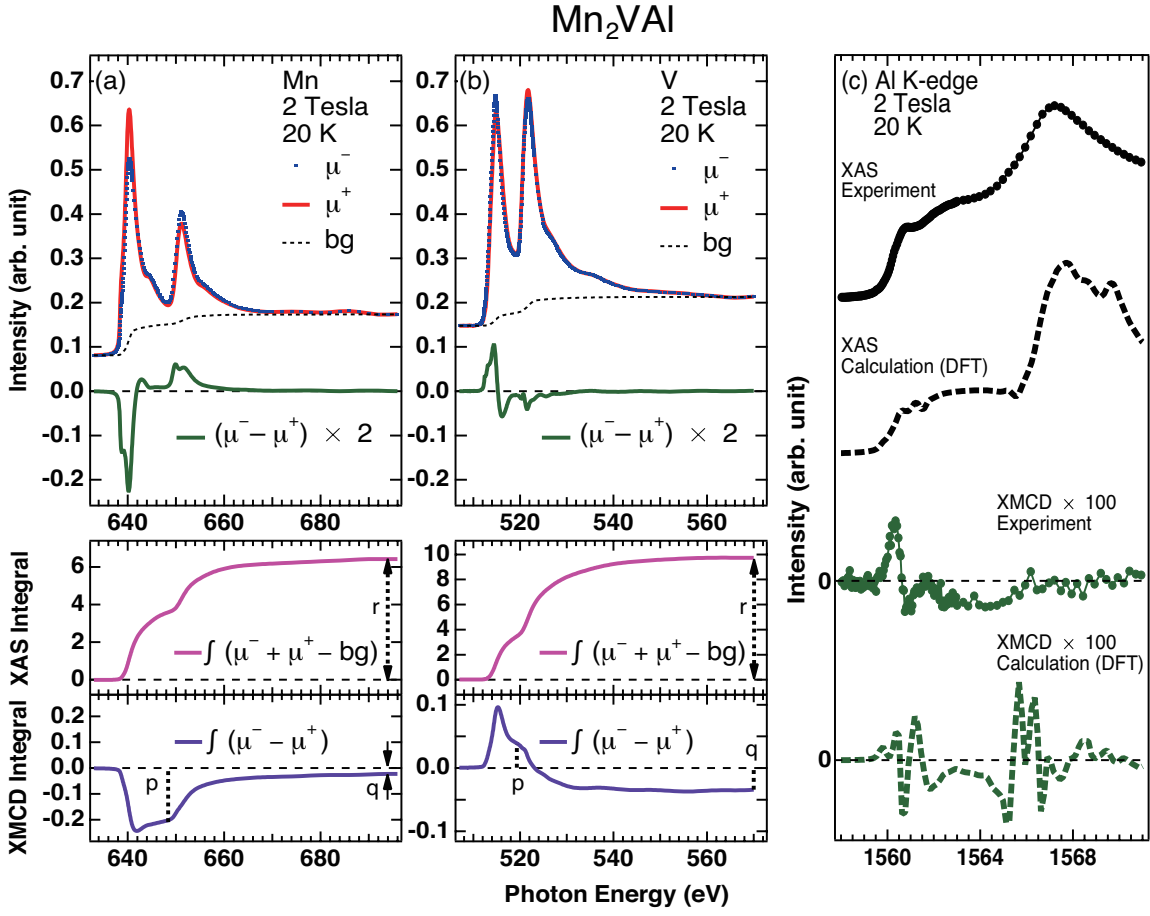


FIG. 2: (Color online) XAS and XMCD spectra of Mn₂VAI recorded at T = 20 K with H = 2 T. (a) Mn and (b) V L_{2,3} XAS and XMCD spectra (top), together with the integrated curves of XAS (middle) and XMCD (bottom). (c) Al K XAS and XMCD spectra with the DFT-based simulation.

TABLE I: Spin and orbital magnetic moments of Mn₂VAI in unit of μ_B per hole for an Mn (V) site obtained by the sum-rule analysis and DFT.

Mn ₂ VAI				
	m_{spin}/n_h (XMCD)	m_{spin}/n_h (DFT)	m_{orb}/n_h (XMCD)	m_{orb}/n_h (DFT)
Mn	0.27	0.28	0.005	0.006
V	-0.15	-0.11	0.005	0.001

spin-orbit splitting at the V L_{2,3} edges [42, 44]. If we evaluate m_{spin}^V using the spin sum-rule assuming C = 1, we obtained $m_{spin}^V = -0.04 \mu_B/\text{V}/\text{hole}$. In this case, we obtained a total V moment of $-0.26 \mu_B/\text{f.u.}$, assuming $n_h = 7.39$ estimated from the DFT. On the other hand, we can evaluate the total V moment as $m^V = -1.04 \mu_B/\text{f.u.}$ using the total Mn moment ($2.86 \mu_B/\text{f.u.}$) and the total bulk moment ($1.82 \mu_B/\text{f.u.}$) obtained by SQUID. Therefore, we found that a likely correction factor for V is C = 3.8, being comparable to that of 3.6 given in Ref. 42. The

spin (orbital) moment for V is deviated from the DFT value of m_{spin}^V (m_{orb}^V) = -0.11 (0.001) $\mu_B/\text{V}/\text{hole}$ as listed in Table I, implying the limitation of DFT for describing the electronic structure of the V 3d states as discussed later.

Figure 3 (a) shows the relative intensity of the Mn L₃ XMCD signal at 640.2 eV on sweeping the field from -2 to 2 T, giving the element specific magnetization profile of the Mn sites. Meanwhile, the field dependence of the V L₃ XMCD intensity at 514.4 eV shows the opposite trend reflecting the antiferromagnetic spin coupling to the Mn moment as shown in Fig. 3(b). The enlarged views around 0 T in the insets of Figs. 3(a) and 3(b) give a coercivity of 10 mT for both Mn and V sites, which is about 10% for the epitaxial films [20]. Moreover, the XMCD intensity does not change after saturating the magnetization, and thus the paramagnetic component reported in Ref. 20 is negligible. Therefore we stress that the impurity and disorder effects are successfully suppressed in our single crystalline samples.

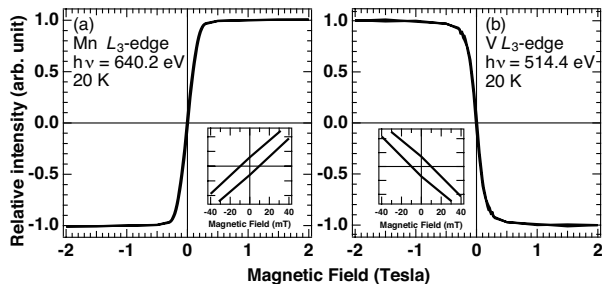


FIG. 3: (Color online) (a), (b) Magnetic field dependence of the XMCD intensity at the Mn and V L_3 peak. The inset shows the expanded view around the 0 T.

XAS and XMCD line shapes: itinerant v.s. localized character in the electronic states

To discuss the characteristic electronic properties of Mn_2VAl , we focus on the detailed line shapes of the polarization-summed XAS and XMCD spectra for both Mn and V $L_{2,3}$ edges. Figure 4(a) displays the enlarged view of the Mn $L_{2,3}$ XAS spectrum of Mn_2VAl , showing a metallic line shape as reported in Ref. 22. Compared with the XAS spectrum of Co_2MnSi , in which the Mn $3d$ states have a localized $3d^5$ character [13, 14, 17], the L_3 main line of Mn_2VAl shifts to higher energies even though the leading edges start at the same energy of 638 eV. Moreover, the L_2 peak of Mn_2VAl does not show the doublet structure due to the atomic multiplets observed in Co_2MnSi [12–14, 17, 46, 47].

In contrast, the XMCD spectrum of Mn_2VAl shows clear doublet peaks in the L_2 edge as well as a clear shoulder structure on the low energy side of the L_3 main peak as shown in Fig. 4(b). This line shape is qualitatively consistent with that reported in Ref. 21. Note that the Mn L_3 XMCD spectrum of Co_2MnSi shows the single peak located at the middle of the L_3 main line in contrast to the low-energy shoulder present in Mn_2VAl , illustrating a clear difference in the local electronic structure on the Mn sites between these two materials.

In Fig. 5 we show the V $L_{2,3}$ XAS and XMCD spectra of Mn_2VAl together with those of V metal reported in Refs. 44 and 48 to discuss the electronic structure of the Y-site element. The V $L_{2,3}$ XAS spectrum of Mn_2VAl is qualitatively similar to that for V metal. Nevertheless, the XMCD spectrum of Mn_2VAl significantly deviates from that of V metal. The single XMCD peak before the L_3 main line observed in V metal is suppressed, while two tiny shoulder structures show up before the L_3 main peak in Mn_2VAl [20, 21]. In addition, the L_2 XMCD shape for Mn_2VAl is clearly different from that of V metal, which is well reproduced by DFT-based simulations [44, 48]. These results suggest the localized character of the V $3d$ states in Mn_2VAl .

To obtain further insight of the electronic structure for the Mn and V $3d$ states, we have analyzed the line shapes

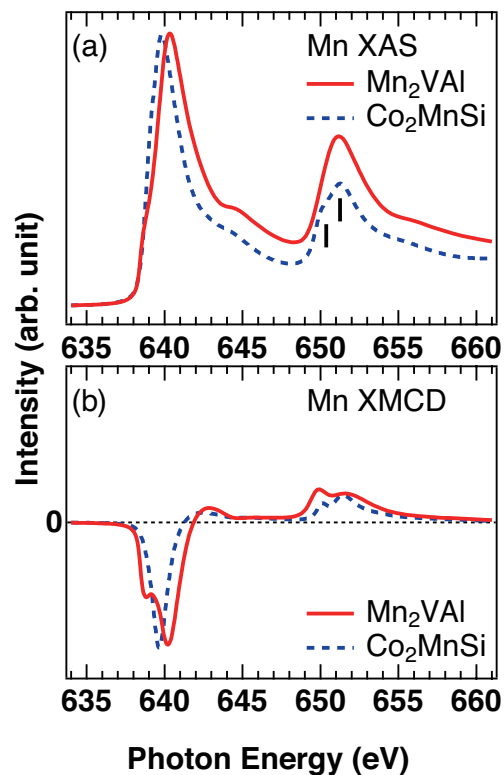


FIG. 4: (Color online) Mn $L_{2,3}$ -edges XAS (a) and XMCD (b) spectra for Mn_2VAl (solid line) and Co_2MnSi (dashed line).

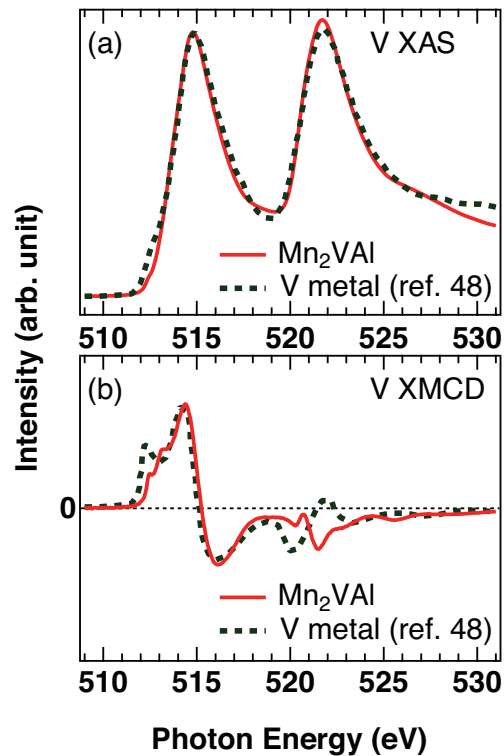


FIG. 5: (Color online) V $L_{2,3}$ -edges XAS (a) and XMCD (b) spectra for Mn_2VAl (solid line) and V metal (dashed line) reported in the reference [48]. The XMCD spectra are normalized at the L_3 peak.

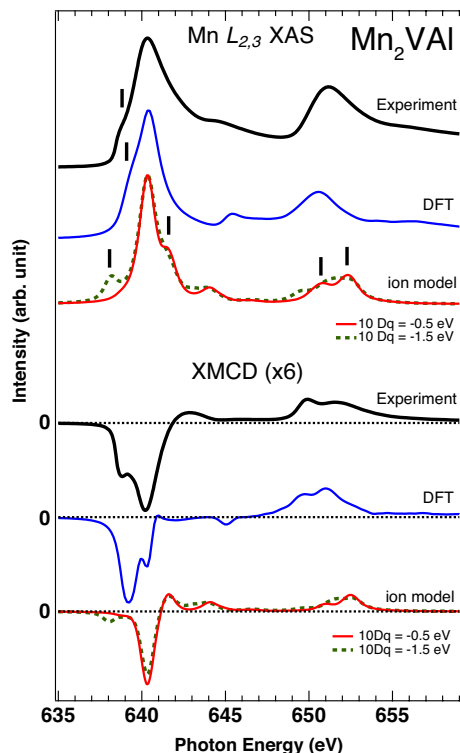


FIG. 6: (Color online) Mn $L_{2,3}$ -edge XAS and XMCD spectra compared with the simulation based on DFT and the ionic model. Spectra are normalized by the L_3 -peak intensity of the polarization summed XAS spectra.

of XAS and XMCD spectra using simulations based on the DFT and the ionic model, representing the itinerant and localized limit of the $3d$ states. The ionic calculations based on the full multiplet theory were implemented using the XTLS 9.0 program [49]. The local crystalline electric field (CEF) was taken into account for the Mn^{2+} ion with tetrahedral (T_d) symmetry and the V^{2+} ion with octahedral (O_h) symmetry. All the intra-atomic parameters such as the $3d$ - $3d$ and $2p$ - $3d$ Coulomb and exchange interactions (Slater integrals) and the $2p$ and $3d$ spin-orbit couplings have been obtained using Cowan's Hartree-Fock code [50] and reducing the Slater parameters to 80%.

In Fig. 6, we show the results of spectral simulations for the Mn $L_{2,3}$ XAS and XMCD. The ionic model XAS calculation with $10Dq = -0.5$ eV [14] shows multiplet structures with a shoulder on the higher energy side of the L_3 main line and the L_2 doublet. Moreover, an additional low-energy satellite at the L_3 peak appeared, reflecting the CEF splitting of $10Dq = -1.5$ eV. However, such multiplet structures are not observed in the experimental XAS spectrum. Furthermore, the XMCD simulation based on the ionic model is obviously deviated from the experimental result, whereas the DFT-based simulation better reproduces the XAS and XMCD spectra, particularly for the low energy structure at the L_3 edge,

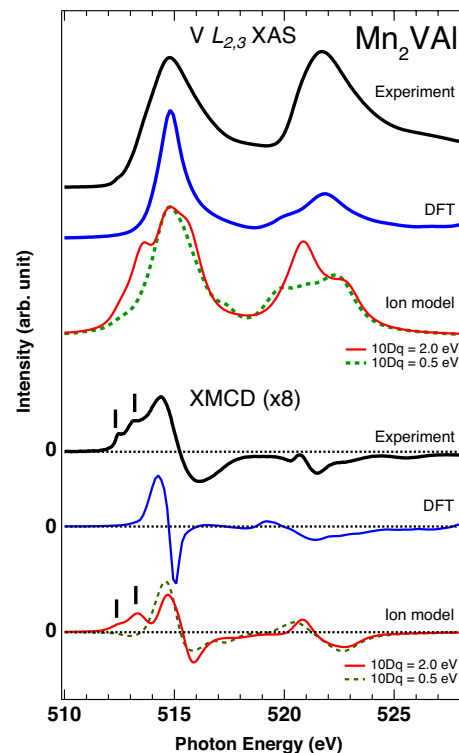


FIG. 7: (Color online) V $L_{2,3}$ -edge XAS and XMCD spectra compared with the simulation based on DFT and the ionic model. Spectra are normalized by the L_3 -peak intensity of the polarization summed XAS spectra.

indicating the itinerant character of the Mn $3d$ states in Mn_2VAI .

On the other hand, the situation is different in the case of V $L_{2,3}$ XAS spectra as shown in Fig. 7. The DFT-based simulation fails to explain the relative peak-intensity ratio of L_3 and L_2 XAS. Moreover, the line shape of XMCD spectrum is not explained by DFT especially for the low-energy shoulders of the L_3 XMCD. In addition, one may also notice that the L_2 XMCD is also deviated from DFT in contrast to the case of V-metal [44, 48] (Fig. 5(b)), implying the limitation of the band picture for the V $3d$ states in the case of Mn_2VAI . Meanwhile, the ionic calculation reproduces the experimental results rather well with a CEF parameter of $10Dq = 2$ eV for O_h symmetry, which is not dramatically smaller than the band-splitting energy between the V $3d$ t_{2g} and e_g states obtained by the DFT as shown in Fig. 1. These results suggest that the V $3d$ electrons are rather localized and thus the atomic multiplets should be taken into account for the spectral simulations.

To check the localized nature of the $3d$ electrons, we have performed Mn and V L_3 RIXS, which is a powerful tool to probe the local electron excitation in the $3d$ states [51, 52]. As shown in Fig. 8(a), the energy-dispersive fluorescence components are dominant in Mn L_3 RIXS, supporting the itinerant picture [53] for the Mn

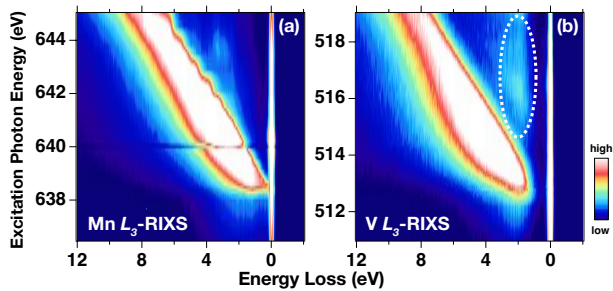


FIG. 8: (Color online) Intensity plots of $h\nu_{in}$ -dependent RIXS at the Mn (a) and V (b) L -edges. Dashed circle is the guide for the eye indicating the resonant excitation.

$3d$ states. Meanwhile, the V L_3 RIXS in Fig. 8(b) clearly shows the clear resonant inelastic excitation (dd excitation) with the constant energy-loss component around 2 eV, which is consistent with the $10Dq$ value of ionic calculations for the V $L_{2,3}$ XAS and XMCD spectra. Therefore, we stress that this dd excitation indicates the localized character of the V $3d$ electrons in Mn_2VAl .

CONCLUSIONS

We investigated the element specific magnetic properties and electronic structure of three different constitute elements of high quality single crystal Mn_2VAl by using XAS and XMCD. The successful observation of the Al K XMCD signals suggests the very small spin unbalance of the Al p states near E_F induced by the hybridization with the transition metal $3d$ states. The Mn and V $L_{2,3}$ edge XMCD spectra show the ferrimagnetic spin coupling between Mn and V states, and the magnetic moments evaluated by the sum-rule analysis has shown an excellent agreement with DFT calculation for its Mn sites. The electronic structure analysis for the Mn $L_{2,3}$ XAS and XMCD spectra with the DFT-based simulation reveals the itinerant character of the Mn $3d$ states, whereas the V $L_{2,3}$ XAS and XMCD spectra are qualitatively explained by the ionic model. In addition, V L_3 RIXS showed the dd excitation, indicating the localized character of the V $3d$ states. Our results give the significant remark to design the magnetic properties by controlling the itinerant and localized character of the d states depending on the site symmetry in Heusler alloys.

ACKNOWLEDGMENTS

We thank T. Kanomata, S. Imada, A. Yamasaki, K. Yamagami, M. Kawada, A. Koide and A. Kimura for fruitful discussions. The measurements were performed under the approval of BL23SU and BL07LSU at SPring-8 (Proposal Nos. 2016A3832 (E28) and 2016B7512). FK,

HF, and TO would like to thank support by Materials research by Information Integration Initiative from CMI²-MaDIS, NIMS. This work was financially supported by a Grant-in Aid for Scientific Research (JP16H04014) from the Ministry of Education, Culture, Sports, Science and Technology, Japan. A part of this work was supported by Japan Science and Technology Agency, Precursory Research for Embryonic Science and Technology (JST-PRESTO).

APPENDIX: OFF-STOICHIOMETRY EFFECTS

The off-stoichiometry effects in Mn_2VAl were numerically simulated by the Korringa-Kohn-Rostoker (KKR) method incorporated with the coherent-potential approximation (CPA) in the local density approximation (LDA) implemented by Machikaneyama-2002 package [54] as demonstrated in Fig. 9. The atomic positions and the lattice constant were set to the same values as Section III. Assuming that the Al sites are substituted by excess ions with 2% for Mn and 8% for V, which is evaluated by EPMA for the measured specimen, we obtained the total magnetic moment of $1.71 \mu_B/f.u.$ This value was smaller than that of the stoichiometric composition of $1.96 \mu_B/f.u.$ The obtained spin polarization at E_F defined as $P = (N_\uparrow - N_\downarrow)/(N_\uparrow + N_\downarrow)$, where N_\uparrow (N_\downarrow) denotes DOS at E_F for the majority (minority) spin subband in Fig. 9, is obtained as -0.93 (-0.91) for off-stoichiometric (stoichiometric) composition. Note that the total density of states are not significantly modified due to the off-stoichiometry effects within the simulation as shown in Fig. 9.

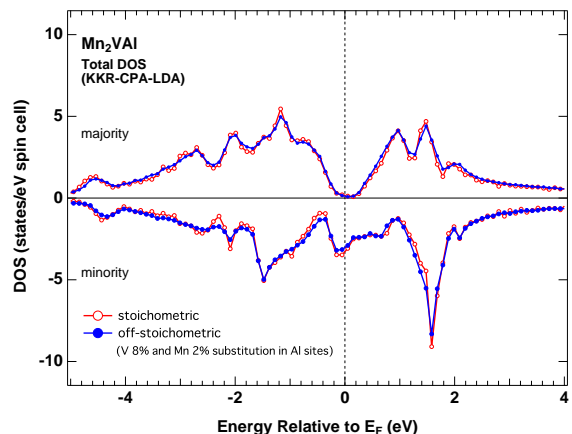


FIG. 9: (Color online) Off-stoichiometric effects on total density of states of Mn_2VAl obtained by the KKR-CPA-LDA method.

-
- * Electronic address: fujiwara@mp.es.osaka-u.ac.jp
- [1] I. Galanakis, in *Heusler Alloys*, edited by C. Felser and A. Hirohata, Springer Series in Materials Science (Springer International Publishing, Switzerland, 2016), Vol. 222.
 - [2] P. J. Brown, K.U. Neumann, P.J. Webster, and K.R.A. Ziebeck, *J. Phys.: Condens. Matter* **12**, 1827 (2000).
 - [3] Y. Yoshida, M. Kawakami, and T. Nakamichi, *J. Phys. Soc. Jpn.* **50**, 2203 (1981).
 - [4] R. Y. Umetsu and T. Kanomata, *Phys. Proc.* **75**, 890 (2015).
 - [5] S. Ishida, S. Asano, and J. Ishida, *J. Phys. Soc. Jpn.* **53**, 2718 (1984).
 - [6] R. Weht and W. E. Pickett, *Phys. Rev. B* **60**, 13006 (1999).
 - [7] C. Jiang, M. Venkatesan, and J.M.D. Coey, *Solid State Commun.* **118**, 513 (2001).
 - [8] L. Ritchie, G. Xiao, Y. Ji, T. Y. Chen, C. L. Chien, M. Zhang, J. Chen, Z. Liu, G. Wu, and X. X. Zhang, *Phys. Rev. B* **68**, 104430 (2003).
 - [9] H. Itoh, T. Nakamichi, Y. Yamaguchi and N. Kazama, *Trans. Jpn. Inst. Met.* **24**, 265, (1983).
 - [10] J. Z. Sun, *Phys. Rev. B* **62**, 570 (2000).
 - [11] A. Yamasaki, S. Imada, R. Arai, H. Utsunomiya, S. Suga, T. Muro, Y. Saitoh, T. Kanomata and S. Ishida, *Phys. Rev. B* **65**, 104410 (2002).
 - [12] K. Miyamoto, K. Ioria, A. Kimura, T. Xie, M. Taniguchi, S. Qiao, and K. Tsuchiya, *Solid State Communications* **128**, 163 (2003).
 - [13] N. D. Telling, P. S. Keatley, G. van der Laan, R. J. Hicken, E. Arenholz, Y. Sakuraba, M. Oogane, Y. Ando, and T. Miyazaki, *Phys. Rev. B* **74**, 224439 (2006).
 - [14] N. D. Telling, P. S. Keatley, G. van der Laan, R. J. Hicken, E. Arenholz, Y. Sakuraba, M. Oogane, Y. Ando, K. Takanashi, A. Sakuma, and T. Miyazaki, *Phys. Rev. B* **78**, 184438 (2008).
 - [15] P. Klaer, M. Kallmayer, H. J. Elmers, L. Basit, J. Thöne, S. Chadov and C. Felser, *J. Phys. D: Appl. Phys.* **42**, 084001 (2009).
 - [16] P. Klaer, E. Arbelo Jorge, M. Jourdan, W. H. Wang, H. Sukegawa, K. Inomata, and H. J. Elmers, *Phys. Rev. B* **82**, 024418 (2010).
 - [17] G. H. Fecher, D. Ebke, S. Ouardi, S. Agrestini, C. Y. Kuo, N. Hollmann, Z. Hu, A. Gloskovskii, F. Yakhou, N. B. Brookes, C. Felser, *SPIN* **04**, 1440017 (2014).
 - [18] M. Jourdan, J. Minár, J. Braun, A. Kronenberg, S. Chadov, B. Balke, A. Gloskovskii, M. Kolbe, H. J. Elmers, G. Schönhense, H. Ebert, C. Felser, and M. Kläui, *Nat. Commun.* **5**, 4974 (2014).
 - [19] M. Tsunekawa, Y. Hattori, A. Sekiyama, H. Fujiwara, S. Suga, T. Muro, T. Kanomata, and S. Imada, *Jpn. J. Appl. Phys.* **54**, 082401 (2015).
 - [20] T. Kubota, K. Kodama, T. Nakamura, Y. Sakuraba, M. Oogane, K. Takanashi, and Y. Ando, *Appl. Phys. Lett.* **95**, 222503 (2009).
 - [21] M. Meinert, J.-M. Schmalhorst, G. Reiss and E. Arenholz, *J. Phys. D: Appl. Phys.* **44**, 215003 (2011).
 - [22] J. Karel, F. Bernardi, C. Wang, R. Stinshoff, N.-O. Born, S. Ouardi, U. Burkhardt, G. H. Fecher and C. Felser, *Phys. Chem. Chem. Phys.* **17**, 31707 (2015).
 - [23] B. T. Thole, P. Carra, F. Sette, and G. van der Laan, *Phys. Rev. Lett.* **68**, 1943 (1992).
 - [24] P. Carra, B. T. Thole, M. Altarelli, and X. Wang, *Phys. Rev. Lett.* **70**, 694 (1993).
 - [25] F. de Groot and A. Kotani, *Core Level Spectroscopy of Solids* (CRC Press, Boca Raton, FL, 2008).
 - [26] L. J. P. Ament, M. van Veenendaal, T. P. Devereaux, J. P. Hill, and J. van den Brink, *Rev. Mod. Phys.* **83**, 705 (2011).
 - [27] P. J. Webster, *J. Phys. Chem. Solids* **32**, 1221 (1971).
 - [28] Y. Takamura, R. Nakane, and S. Sugahara, *J. Appl. Phys.* **105**, 07B109 (2009).
 - [29] Y. Saitoh, Y. Fukuda, Y. Takeda, H. Yamagami, S. Takahashi, Y. Asano, T. Hara, K. Shirasawa, M. Takeuchi, T. Tanaka, and H. Kitamura, *J. Synchrotron Rad.* **19**, 388 (2012).
 - [30] Y. Harada, M. Kobayashi, H. Niwa, Y. Senba, H. Ohashi, T. Tokushima, Y. Horikawa, S. Shin, and M. Oshima, *Rev. Sci. Instrum.* **83**, 013116 (2012).
 - [31] S. Yamamoto, Y. Senba, T. Tanaka, H. Ohashi, T. Hirano, H. Kimura, M. Fujisawa, J. Miyawaki, A. Hara-sawa, T. Seike, S. Takahashi, N. Nariyama, T. Matsushita, M. Takeuchi, T. Ohata, Y. Furukawa, K. Takeshita, S. Goto, Y. Harada, S. Shin, H. Kitamura, A. Kakizaki, M. Oshima and I. Matsuda, *J. Synchrotron Rad.* **21**, 352, (2014).
 - [32] J. Miyawaki, S. Suga, H. Fujiwara, H. Niwa, H. Kiuchi and Y. Harada, *J. Synchrotron Rad.* **24**, 449 (2017).
 - [33] E. Wimmer, H. Krakauer, M. Weinert, and A. J. Freeman, *Phys. Rev. B* **24**, 864 (1981).
 - [34] J. P. Perdew, K. Burke, and M. Ernzerhof, *Phys. Rev. Lett.* **77**, 3865 (1996).
 - [35] J. P. Perdew, K. Burke, and M. Ernzerhof, *Phys. Rev. Lett.* **78**, 1396 (1997).
 - [36] H. Fujii, M. Toyoda, H. Momida, M. Mizumaki, S. Kimura, and T. Oguchi, *Phys. Rev. B* **90**, 014430 (2014).
 - [37] J. Schmalhorst, A. Thomas, S. Kämmerer, O. Schebaum, D. Ebke, M. D. Sacher, G. Reiss, A. Hütten, A. Turchanin, A. Götzhäuser and E. Arenholz, *Phys. Rev. B* **75**, 014403 (2007).
 - [38] R. Y. Umetsu, T. Kanomata, K. Kobayashi, R. Kainuma, A. Sakuma, K. Fukamichi and K. Ishida, *J. Phys. D: Appl. Phys.* **43**, 105001 (2010).
 - [39] G. Y. Guo, *J. Phys.: Condens. Matter* **8**, L747 (1996).
 - [40] G. van der Laan and A. I. Figueroa, *Coord. Chem. Rev.* **277**, 95 (2014).
 - [41] K. Edmonds, G. van der Laan and G. Panaccione, *Semicond. Sci. Technol.* **30**, 043001 (2015).
 - [42] E. Goering, *Phil. Mag.* **85**, 2895 (2005).
 - [43] H. A. Dürr, G. van der Laan, D. Spanke, F. U. Hillebrecht and N. B. Brookes, *Phys. Rev. B* **56**, 8156 (1997).
 - [44] A. Scherz, H. Wende, K. Baberschke, J. Minár, D. Benea, and H. Ebert, *Phys. Rev. B* **66**, 184401 (2002).
 - [45] C. Piamonteze, P. Miedema and F. M. F. de Groot, *Phys. Rev. B* **80**, 184410 (2009).
 - [46] A. Kimura, S. Suga, T. Shishidou, S. Imada, T. Muro, S. Y. Park, T. Miyahara, T. Kaneko and T. Kanomata, *Phys. Rev. B* **56**, 6021 (1997).
 - [47] B. T. Thole, R. D. Cowan, G. A. Sawatzky, J. Fink and J. C. Fuggle, *Phys. Rev. B* **31**, 6856 (1985).
 - [48] H. Wende, *Rep. Prog. Phys.* **67**, 2105 (2004).
 - [49] A. Tanaka and T. Jo, *J. Phys. Soc. Jpn.* **63**, 2788 (1994).
 - [50] R. D. Cowan, *The Theory of Atomic Structure and Spectra* (University of California Press, Berkeley, CA, 1981).
 - [51] G. Ghiringhelli, M. Matsubara, C. Dallera, F. Fracassi, A. Tagliaferri, N. B. Brookes, A. Kotani, and L.

- Braicovich, Phys. Rev. B **73**, 035111 (2006).
- [52] E. Benckiser, L. Fels, G. Ghiringhelli, M. Moretti Sala, T. Schmitt, J. Schlappa, V. N. Strocov, N. Mufti, G. R. Blake, A. A. Nugroho, T. T. M. Palstra, M. W. Haverkort, K. Wohlfeld, and M. Grüninger, Phys. Rev. B **88**, 205115 (2013).
- [53] W. L. Yang, A. P. Sorini, C-C. Chen, B. Moritz, W.-S. Lee, F. Vernay, P. Olalde-Velasco, J. D. Denlinger, B. Delley, J.-H. Chu, J. G. Analytis, I. R. Fisher, Z. A. Ren, J. Yang, W. Lu, Z. X. Zhao, J. van den Brink, Z. Hussain, Z.-X. Shen, and T. P. Devereaux, Phys. Rev. B **80**, 014508 (2009).
- [54] H. Akai, J. Phys.: Condens. Matter **1**, 8045 (1989).